PERGAMON

Continental Shelf Research 18 (1998) 561–584

CONTINENTAL SHELF RESEARCH

Tidal currents in a topographically complex channel

Andreas Münchow

Institute of Marine and Coastal Sciences, Rutgers University, 71 Dudley Rd., New Brunswick, NJ 08901-8521, USA

Received 27 February 1997; accepted 30 December 1997

Abstract

The Santa Barbara Channel off Southern California constitutes a topographically complex channel that is open at both ends. Tidal sea level oscillations are well explained by a northwestward propagating Kelvin wave. Tidal currents vary at a multitude of topographic and temporal scales and cannot be explained by linear Kelvin wave dynamics alone. The analysis reveals three regions with distinctly different tidal currents. In the deep central basin and along a narrow northern shelf tidal currents are weak (<5 cm/s) while at the eastern channel entrance they are enhanced (15 cm/s). In a third region, tidal currents are particular strong (>30 cm/s) and tidal particle excursions are similar to the shelf width. Applying spectral and harmonic data analysis techniques, I distinguish between predictable (62% of the variance) and intermittent (38% of the variance) tidal currents. More than 94% of the latter are baroclinic, while the variance of the predictable tidal currents is equally distributed between baroclinic and barotropic motions. Two empirical orthogonal functions explain 87% for the predictable but only 61% of the intermittent baroclinic variance. Intermittent tidal currents vary little in space and can reach 15 cm/s in amplitude during a 2-day period, however, in the temporal mean these unpredictable tidal current are only 5 cm/s. In contrast, the predictable tidal currents vary in space from 5 to 50 cm/s during any 2-day period.

1. Introduction

In 1926 tidal current observations settled an old argument on the existence of an ice-covered continent over the North Pole. Harald Sverdrup, a young Norwegian oceanographer, concluded the debate after he returned from a 3 year-long Arctic expedition. He used tidal theory together with tidal current and sea level observations along the path of his sailing vessel *Maud* to conclude correctly that no land mass existed in the Arctic Ocean (Sverdrup, 1926). Sverdrup's success constitutes the first application of modern tidal current measurements.

0278-4343/98/$19.00
PII S0278-4343(97)00008-9

Tidal currents constitute the most ubiquitous signal in the coastal ocean. They can be difficult to interpret as they vary at a multitude of topographic scales. In contrast, tidal sealevel oscillations vary significantly only at the largest topographic scale. Kelvin wave dynamics often predict the evolution of sea level oscillations well, however, the same is not true for tidal currents. Taylor (1921) represents tides as Kelvin waves that reflect at the head of the embayment. Hendershott and Speranza (1971) expand this model by including friction in the form of a Kelvin wave that reflects only a fraction of its energy at the head of the embayment. Their analytical results compare favorably with observations from the Gulf of California. Battisti and Clarke (1982) concentrate on the prediction of tidal current ellipses on continental shelves. They find analytically that the major axes of the rotating tidal currents are aligned across topography on wide shelves such as the Atlantic coast of the USA. In contrast, major axes of tidal currents are parallel to the shore on narrow shelves such as those of the Pacific coast of the USA. The predictions agree well with current observations from outer- and mid-shelf regions away from topographic perturbations. On inner shelves, however, topographic irregularities add complications to the dynamics. Münchow et al. (1992a) find that an estuary such as Delaware Bay can enhance tidal currents by a factor of 4 on the shelf more than 20 km away from the estuary.

Zimmerman (1986) reviews the literature on shear dispersion and Lagrangian chaos in tidally dominated flow fields. Both mixing processes require spatial gradients in tidal properties. Advection of tidally generated vorticity can generate mean flows (Zimmerman, 1981), hence spatially variable tidal currents relate both to mixing and mean flow generation. Geyer and Signell (1990) report spatially variable tidal and residual current observations near a headland on Martha's Vinyard, Massachussetts. They report strong tidal currents that generate residual eddies near the headland. The spatial variability of tidal currents introduces nonlinearities in the tidal momentum balance through the advective terms. Nonlinearities can transfer energy from tidal to both higher (Aubrey and Speer, 1985) and lower frequency (Münchow et al., 1992a) motions. Much recent interest in tidal currents, however, relates to shipborne ADCP surveys. While the primary goal of most ADCP surveys is to map subtidal currents, the resulting maps are always biased by tidal currents. Foreman and Freeland (1991), Candela et al. (1992), and Münchow et al. (1992b) all struggle to detide spatial ADCP records. Any prior knowledge on the spatial character of tidal currents within a study area helps to properly detide such records. Intermittent internal tidal currents add to the complications.

Gill (1982) explains the generation of internal tides as vortex tube stretching that transfers tidal energy from the barotropic to the baroclinic tide in the presence of vertical stratification, topography, and an across-shelf flow. Initially, the internal tide is phase locked to the generating barotropic tide. As the internal tide propagates away from its generation region, however, it passes through water of variable stratification, variable depth, and is Doppler shifted by ambient subtidal currents (Wunsch, 1975). Eventually, the internal tide looses "memory" of its generation region and becomes intermittent. It is no longer phase-locked to the barotropic tide and constitutes ambient noise near the tidal frequencies. Most continental shelves are both vertically

stratified and sloping and thus support internal tidal motions. Torgrimson and Hickey (1979) present data from a current meter section off Oregon where they find an internal semi-diurnal tide that is generated near the shelf break. The tide reflects from both surface and bottom as it propagates along characteristics towards the coast. Leaman (1980) reports a strong diurnal internal tide on the wide West Florida shelf that propagates onshore also. In contrast to Torgrimson and Hickey (1979), however, he did not find a propagation pathway along narrow well-defined characteristics. Rosenfeld (1990) presents modern internal tide observations from the northern California shelf. She finds that internal tidal currents in the CODE region are intermittent in both time and space. Correlation scales are short, about 20–40 km both across and along the shelf. Using Topex/Poseidon satellite altimeter data, Ray and Mitchum (1996) report much longer correlation scales of short wavelength, phase-locked tidal surface elevation that they associate with an internal tide generated in the vicinity of the Hawaiian Ridge.

2. Study area and data sources

We here report tidal current and sea level oscillations from the Santa Barbara Channel off the coast of southern California. The Santa Barbara Channel facilitates both off-shore oil exploration and suburban recreation. It is the site of the Channel Island National Park. The channel is about 30 km wide and extends about 150 km east–west with a 10 km wide entrance in the east and a 40 km wide opening in the west (Fig. 1). Two sills separate a 600 m deep central basin from ambient waters. The eastern sill is about 200 m deep while the western sill depth exceeds 400 m just south of Point Conception. The California coastline constitutes the northern boundary of the channel while a chain of four islands separates the channel to the south from the larger and deeper Santa Monica and Santa Cruz basins. The passages between the islands and the basins to the south are less than 10 km wide, less than 50 m deep, and are the locale of intense tidal currents. Defining the 100 m isobath as the outer edge of the continental shelf, I find that the deep basin of the Santa Barbara Channel is bordered by a northern and a southern shelf which vary in width between 5 and 20 km. The Santa Barbara Channel thus constitutes a topographically complex system of shelves,

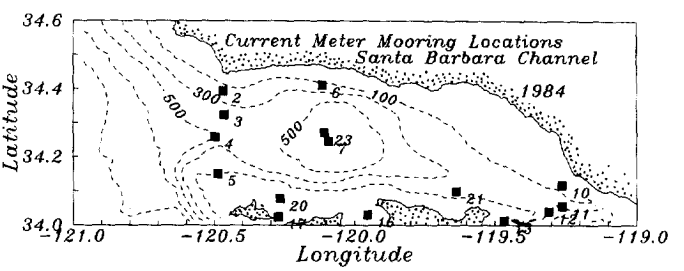

Fig. 1. Map of the study area, bottom topography, and instrument locations.

sills, channels, and a deep basin. These bathymetric complexities result in tidal currents that vary at a multitude of topographic scales.

For the description of tidal sea level and current oscillations I use data from subsurface pressure sensors, coastal tide gauges, and moored current meters. Tide gauges are operated by NOS along the coast while six subsurface pressure sensors

Table 1
1984 current meters locations in the Santa Barbara Channel. The mooring name refers to the location of the mooring, i.e., W refers to the western entrance, E to the eastern entrance, S to the southern shelf, and C to the central basin

Mooring (Station)	Latitude North (degrees)	Longitude West (degrees)	Water depth (m)	Instrument depth (m)	Record length (days)
W1 (02)	34.394	120.471	150	30	332
				100	323
W2 (03)	34.325	120.466	366	30	285
				100	157
				200	174
				350	287
W3 (04)	34.259	120.499	476	30	174
				100	174
				250	174
W4 (24)	34.152	120.486	87	8	227
(05)	34.151	120.488	90	30	344
				65	344
C1 (06)	34.411	120.117	178	30	294
				105	316
C2 (23)	34.270	120.108	565	8	323
(07)	34.246	120.095	599	30	288
				105	236
				538	330
E1 (10)	34.118	119.264	27	21	221
(11)	34.056	119.264	346	76	330
				126	330
				176	330
				246	158
E2 (12)	34.041	119.310	98	30	228
				80	320
E3 (13)	34.013	119.468	54	30	229
				45	168
S1 (20)	34.078	120.268	73	30	332
				65	332
S3 (21)	34.100	119.638	180	30	334
				80	334
S2 (16)	34.031	119.956	44	25	266
				38	299
S4 (17)	34.025	120.273	35	25	225
				28	179

were deployed and maintained by the Scripps Institution of Oceanography since 1992. More than 35 current meters were deployed at 15 locations in the Santa Barbara Channel in 1984 (Gunn et al., 1987). Their record length varies from 157 to 344 days, the average record length is 268 days (Table 1). A similar array was deployed in a pilot study in 1983 (Brink and Muench, 1986), however, the records then were only 62 days long. The locations of the 1984 current meter moorings are shown in Fig. 1. The 1983 moorings were deployed at almost identical locations (not shown). All data were high-pass filtered with a Lanczos filter that has its half-power point near 0.5 cpd. The filter passed more than 90% and less than 10% of the variance at periods near 1 and 2 days, respectively.

3. Methodology

Sea level oscillations are affected little by internal oscillations except in extreme cases where the baroclinic tidal currents generate seiche motions (Giese and Hollander, 1987). Such motions are not present in the study area and I thus interpret the tidal sea level oscillations as caused solely by the barotropic tidal currents. In order to separate the intermittent motions from those that are phase locked to the barotropic tide, I subject all current meter data to a frequency domain linear system analysis (Bendat and Piersol, 1978). The analysis decomposes the velocity record (u, v) in the frequency domain into a portion $(Tf_u, Tf_v)^*\eta$ that is coherent with local sea level η and a portion ψ that is incoherent with local sea level oscillations, i.e.,

$$(u, v) = (Tf_u, Tf_v)^*\eta + (\psi_u, \psi_v). \tag{1}$$

Here $(u, v) = (u(f), v(f))$ and $\eta = \eta(f)$ are the Fourier transforms of the velocity and sea levels time series, respectively, while $Tf_u(f)$ and $Tf_v(f)$ are the linear transfer function between velocity components u (east), v (north) and sea level η, and f is a frequency. Noble et al. (1987) applied a similar technique to estimate tidal currents over the slope and deep basin off Northern California. In contrast to their analysis, however, I here transform all 4 terms on the right-hand side of Eq. (1) back into the time domain in order to apply time domain analysis techniques. The sea level coherent data $(Tf_u, Tf_v)^*\eta$ contains the tidal currents that are phase-locked to the barotropic surface tide. Hence, it contains both the barotropic tidal currents and the phase-locked part of the baroclinic tidal currents. The phase-locked baroclinic tidal current is deterministic and thus predictable in the sense that it can be reconstructed from sea level observations. Throughout this study the terms "predictable" and "deterministic" refer to the presence of a transfer function. Predictable and deterministic currents thus include both a barotropic and a baroclinic part. I then interpret the depth average of the predictable currents as the barotropic motions while the deviation from this depth-averaged current constitutes the baroclinic motions. Similarly, the intermittent currents are decomposed into baroclinic and barotropic contributions also.

Fig. 2 shows an example of this separation as it depicts the spectral density distribution of current meter W2 at 30 m below the surface. The original data (Fig. 2a)

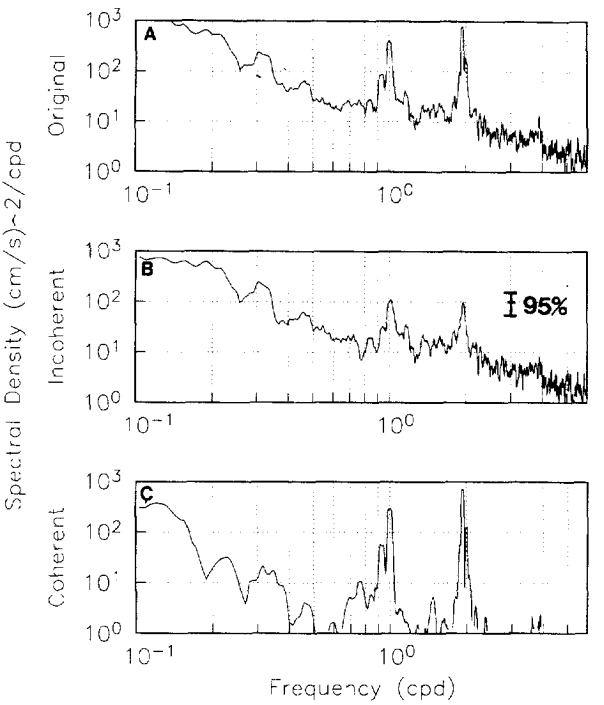

Fig. 2. Spectral density spectra for (a) raw, (b) sea level incoherent, and (c) sea level coherent data. The data originate from the surface instrument (30 m depth) at mooring W2 (station 3 in Fig. 1).

reveal statistically significant (95% confidence) peaks in both the diurnal and the semi-diurnal frequency band. A weak spectral peak is discernible at the quarter diurnal frequency (4 cpd), however, the signal is almost two orders of magnitude smaller than the signal at the principal diurnal and semi-diurnal frequencies. We thus neglect overtides in this study and concentrate on the diurnal and semi-diurnal tidal currents only. The spectral peaks of the diurnal and semi-diurnal tidal currents are surrounded by broad spectral cusps that result from the Doppler shifted intermittent tidal currents (Munk et al., 1970). The cusps of the intermittent tidal currents become particularly clear in Fig. 2b which shows the spectral density distribution of the velocity data that are not coherent with the sea level. Note also that the amplitudes are much reduced in the tidal frequency bands as compared with both the original (Fig. 2a) and the sea level coherent (Fig. 2c) data. The sea level coherent part of the velocity record (Fig. 2c) reveals sharp tidal spectral lines that are several orders of magnitude above a much reduced noise floor of about 1 $(cm/s)^2/cpd$. I interpret these spectral lines as the predictable tidal currents.

Harmonic analysis fits sinusoidal tidal constituents to the data using the method of least squares. In the presence of white, Gaussian noise a sinusoidal signal with

amplitude S_0 and phase ϕ is estimated with an uncertainty (Helstrom, 1960)

$$\mathrm{Var}(S_0) = (S_0/\mathrm{SNR})^2, \tag{2a}$$

$$\mathrm{Var}(\phi) = \mathrm{SNR}^{-1}, \tag{2b}$$

where Var(•) is the variance of the uncertainty and SNR is the signal to noise ratio

$$\mathrm{SNR} = S_0(T/N)^{-1/2}, \tag{3}$$

T is the record length, and N is the noise spectral density at the frequency of the signal. Münchow et al. (1992a) compare the above error estimation technique with others and evaluate the performance of the different methods in controlled numerical experiments. Error estimation techniques depend on SNR and removal of the noisy intermittent tidal currents from the record increases the confidence of estimated parameters. The removal of the sea level incoherent signal thus increases the confidence with which we estimate the amplitudes and phases of the predictable tidal currents.

The central limit theorem specifies that if a random variable $u(t)$ is the sum of mutually independent random variables, i.e.,

$$u(t) = u^{\mathrm{c}} + u_{\mathrm{e}}^{\mathrm{i}} + u_{\mathrm{i}}^{\mathrm{i}} \tag{4}$$

then the variance Var(u) is (Bendat and Piersol, 1986)

$$\mathrm{Var}(u) = \mathrm{Var}(u^{\mathrm{c}} = u_{\mathrm{e}}^{\mathrm{c}} + u_{\mathrm{i}}^{\mathrm{c}}) + \mathrm{Var}(u_{\mathrm{e}}^{\mathrm{i}}) + \mathrm{Var}(u_{\mathrm{i}}^{\mathrm{i}}) \tag{5}$$

where $u_{\mathrm{e}}^{\mathrm{c}}$, $u_{\mathrm{e}}^{\mathrm{i}}$, $u_{\mathrm{i}}^{\mathrm{c}}$, and $u_{\mathrm{i}}^{\mathrm{i}}$ are the external (barotropic) coherent, the external incoherent, the internal (baroclinic) coherent, and the internal incoherent components of the original velocity time series $u(t)$, respectively. The variance of the sea level coherent current u^{c} cannot be decomposed in Eq. (5) because $u_{\mathrm{e}}^{\mathrm{c}}$ and $u_{\mathrm{i}}^{\mathrm{c}}$ are not necessarily independent random variables. They both correlate with local sea level. Estimating the variances for each term $u_{\mathrm{e}}^{\mathrm{c}}$, $u_{\mathrm{e}}^{\mathrm{i}}$, $u_{\mathrm{i}}^{\mathrm{c}}$, and $u_{\mathrm{i}}^{\mathrm{i}}$ individually below, however, I will find that $V(u^{\mathrm{c}}) = V(u_{\mathrm{e}}^{\mathrm{c}}) + V(u_{\mathrm{i}}^{\mathrm{c}})$. Hence all 4 components of the current are accounted for in the case that an appropriate depth averaged current can be formed. This, however, is not always possible. Initially, I though that an empirical orthogonal function (EOF) analysis would separate barotropic from baroclinic motions, however, numerical test cases proved this approach deficient. An EOF analysis always decomposes the currents into modes whose time series are approximately 90° out of phase. Even a barotropic oscillation at a frequency different from that of a baroclinic oscillation results into two apparent baroclinic eigen-modes. Each mode contains signals at both frequencies. The vertical average of a sufficient number of current observation in the vertical thus must be used to define the barotropic current. Below I thus use EOF analysis only to order the vertical variability in the tidal frequency band.

4. Sea level

Tidal elevations along the narrow shelves of the U.S. West Coast are dominated by a northward propagating Kelvin wave (Munk et al., 1970). The phases of both

M_2 (Fig. 3) and K_1 (not shown) surface tide vary smoothly from the eastern to the western entrance of the channel. The phase difference along the channel is about 20° and 10° for the M_2 and K_1 tide, respectively, i.e., high water occurs at the eastern entrance about 40 min before it occurs on the western entrance. The ratio of the dominant semi-diurnal to diurnal sea level amplitudes, i.e., $(M_2 + S_2)/(K_1 + O_1)$ is about 1.13 and the tidal sea level is thus of the mixed diurnal/semi-diurnal type.

At the eastern entrance of the Santa Barbara Channel the M_2 sea level amplitude varies smoothly from 0.50 m on the northern shelf to 0.45 m off Anacapa Island to the South (Fig. 3). Garrett and Petrie (1981) and Münchow et al. (1992a) find similar sea level difference across the Strait of Belle Isle and the mouth of the Delaware Estuary, respectively. Garrett and Petrie (1981) explained this feature as a geostrophic adjustment to currents that are stronger on one side of a curving channel while Münchow et al. (1992) referred to bottom friction and variable bottom depth as the cause for sea level and current gradients across the mouth of an estuary. Neither of these processes applies to the Santa Barbara Channel. Largest tidal currents occur near Anacapa Islands where the sea level amplitude is the smallest. Furthermore, the water is more than 100 m deep, too deep for friction to influence the entire water column.

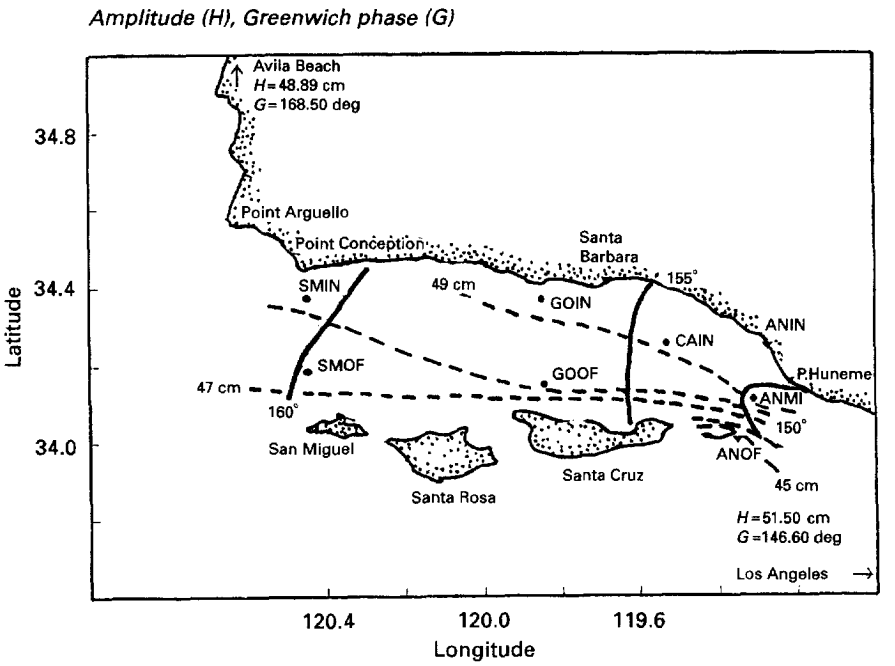

Fig. 3. Map of the M_2 sea level oscillations in the Santa Barbara Channel from both coastal tide gauge stations and subsurface pressure gauges. Solid and broken curves are cotidal (Greenwich phase) and co-range (cm) lines.

5. Tidal currents

Here, I report results from harmonic analysis of the deterministic records, derived as described above. Tidal currents in the Santa Barbara Channel vary in their composition (diurnal vs. semi-diurnal) as well as in the horizontal and vertical dimensions. A composite of this variability is shown in Fig. 4. It depicts the amplitude ratio ε between the two dominant semi-diurnal M_2 and S_2 currents and the two dominant diurnal K_1 and O_1 currents across the western entrance to the south of Point Conception (see Fig. 1 for locations), i.e.,

$$\varepsilon = (M_2 + S_2)/(K_1 + O_1). \tag{6}$$

Tidal currents in the south are dominantly diurnal as diurnal amplitudes exceed semi-diurnal ones by a factor of 5. Over the center of the channel entrance diurnal and semi-diurnal tidal currents are of equal strength, while in the north they are dominantly semi-diurnal. A transition of the character of the tidal current oscillations thus becomes evident as ε ranges from 0.2 to 1.8.

5.1. Horizontal variability

The results of the harmonic analysis of the 1984 current data are shown in Figs. 5 and 6. They depict major and minor axes of current ellipses for the dominant semi-diurnal M_2 (Fig. 5) and the dominant diurnal K_1 tide (Fig. 6) at all measured depths. The maps (Figs. 5a and 6a) emphasize the horizontal variability in ellipse

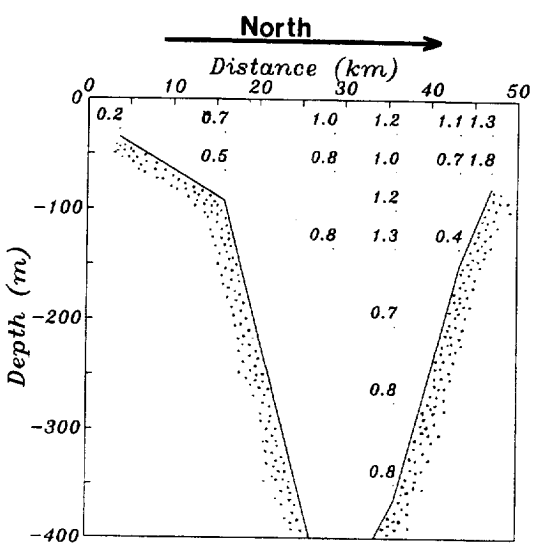

Fig. 4. Ratio of semi-diurnal to diurnal current amplitudes across the western channel entrance (see Fig. 1 for the location of stations 2, 3, 4, 5, 20, and 17).

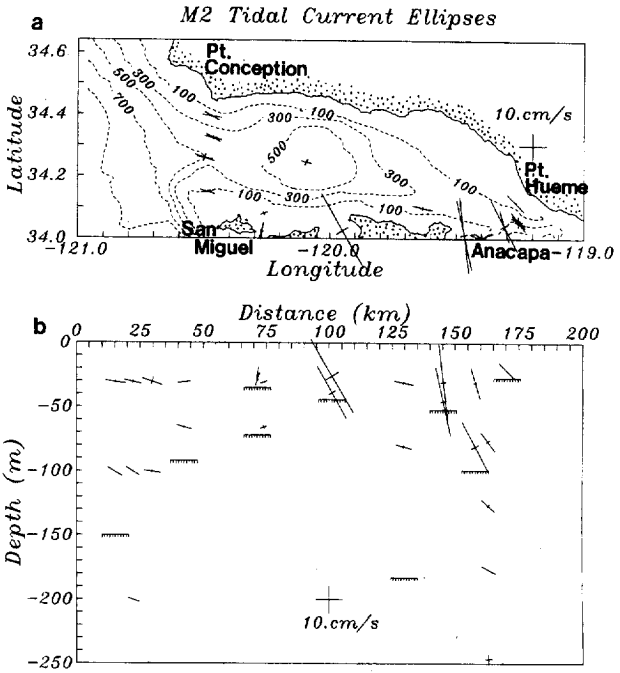

Fig. 5. Major and minor axes of the M_2 tidal current ellipses as (a) a function of horizontal location and (b) a function of depth. The distance in (b) is measured from Point Conception to San Miguel, Anacapa, and to Point Hueme. The bottom at each location is indicated.

parameters while the transects (Figs. 5b and 6b) emphasizes the vertical variability of the same parameters. The sections extend from the northwestern corner of the channel at Point Conception (0 km) to the southwestern corner off San Miguel Island (70 km), along the southern shelf to the southeastern corner off Anacapa Island (150 km) across the eastern channel entrance to the northeastern corner off Point Hueme (175 km). Tables 2 and 3 list the ellipse parameters, their uncertainties, and the signal to noise ratios of the M_2 and K_1 currents, respectively. For both constituents the current ellipses are almost rectilinear, generally rotate clockwise due to the earth's rotation, and align their semi-major axis along contours of bottom topography. They show little variations with depth except near the bottom where the current amplitudes are reduced, presumably by bottom friction. Inside the channel currents are always less than 5 cm/s. In contrast, on the northern shelf they vary between 5 and 10 cm/s. Small tidal currents occur where the shelf is narrow while larger tidal currents occur near Point Conception. Largest current amplitudes occur at the eastern entrance ($\sim$15 cm/s) and in the inter-island passages ($\sim$25 cm/s). Tidal currents reduce rapidly away from the passages. Nevertheless, currents on the southern shelf are always larger than those on the northern shelf. Tidal currents at both diurnal and semi-diurnal frequencies are thus enhanced on the southern shelf.

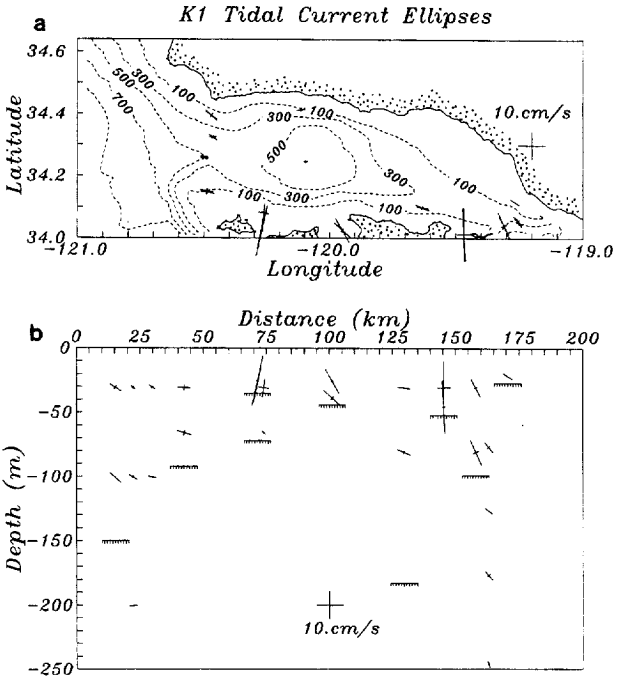

Fig. 6. As Fig. 5 but for the K_1 currents.

The combined effect of all ellipse parameters on the instantaneous currents is best visualized by presenting snapshots of the predicted tidal currents. Fig. 7 maps the M_2 tidal currents in the upper water column ($z < 50$ m) at four different times for half the tidal M_2 cycle. Currents for the other half cycle have the same magnitude but opposite direction. At the time of high water at Santa Barbara (phase $\theta = 0°$) the tidal flow is into the channel in the east while it is out of the channel in the south and west (Fig. 7a). Flows are at their maximum then (Fig. 7a). As sea level falls ($\theta = 45°$) currents are somewhat reduced (Fig. 7b). About 3.1 h after high water ($\theta = 90°$) the currents are generally weak and have changed direction in the east and south but not in the west (Fig. 7c). Hence all currents are out of the channel at this time of maximum sea level drop. Just prior to low water ($\theta = 135°$) the tidal flow is accelerating with flow out of the channel in the east and south and into the channel in the west (Fig. 7d). The apparent in-phase relation of currents and sea level indicates a progressive tidal wave that passes the channel from east to west. It is consistent with a Kelvin wave that propagates through the Santa Barbara Channel from the southeast to the northwest.

Throughout the domain the semi-diurnal currents are about as large as the diurnal currents. At the location of the western most inter-island passage, however, diurnal currents are about 5 times as strong as the semi-diurnal currents (Figs. 4–6). The resulting particle displacement $\delta = UT/\pi$ is about 5 km for a current with an amplitude U of 20 cm/s at a period T of 23.93 h (K_1). This tidal excursion constitutes

Table 2
Tidal ellipse parameters for the M_2 currents in the Santa Barbara Channel. RMAJ indicates the semi-major axis and EPS represents the ratio between semi-minor and semi-major. A positive value for EPS indicates counter-clockwise rotation of current vectors. The orientation of the major axis is measured from true East positive counter-clockwise. The phase angle, finally, indicates the orientation of a current vector at the time of M_2 high water in Santa Barbara (see Münchow et al. (1992a) for a detailed definition). The mooring name refers to the location of the mooring, i.e., W refers to the western entrance, E to the eastern entrance, S to the southern shelf, and C to the central basin

Mooring (Station)	Instrument depth (m)	RMAJ (cm/s)	EPS (%)	Major axis orientation (degrees)	Phase (degrees)	Signal to noise ratio
W1 (02)	30	7.5 ± 1.4	− 9	− 9 ± 10	138	49
	100	6.0 ± 1.2	− 1	− 29 ± 10	193	21
W2 (03)	30	6.1 ± 1.6	− 12	− 14 ± 13	167	95
	100	5.8 ± 1.4	− 8	− 30 ± 13	168	14
	200	4.5 ± 1.6	− 4	− 22 ± 17	157	16
	350	2.5 ± 0.6	48	5 ± 14	145	8
W3 (04)	30	7.4 ± 1.9	− 37	− 21 ± 12	183	27
	100	6.0 ± 2.0	− 14	− 7 ± 14	190	24
	250	4.1 ± 2.0	− 5	− 12 ± 24	165	30
W4 (24)	8	4.5 ± 0.7	− 13	31 ± 11	148	8
(05)	30	4.4 ± 1.2	− 7	8 ± 21	139	14
	65	5.6 ± 1.5	− 11	− 16 ± 12	191	53
C1 (06)	30	1.1 ± 0.3	− 9	− 14 ± 11	207	15
	105	0.8 ± 0.0	20	− 38 ± 00	187	2
C2 (23)	8	3.5 ± 0.9	− 67	6 ± 15	183	11
(07)	30	3.8 ± 0.6	− 50	− 15 ± 09	169	40
	105	3.2 ± 0.7	− 26	− 8 ± 12	165	16
	538	2.2 ± 0.6	3	56 ± 22	141	4
E1 (10)	21	8.3 ± 0.0	5	136 ± 00	11	17
(11)	76	8.2 ± 0.8	− 20	125 ± 04	19	18
	126	6.4 ± 0.2	20	136 ± 02	− 12	16
	176	5.8 ± 1.1	4	153 ± 09	− 19	22
	246	3.8 ± 1.0	− 71	91 ± 15	− 14	5
E2 (12)	30	12.0 ± 2.0	− 8	107 ± 08	2	19
	80	20.8 ± 2.9	− 14	118 ± 07	− 8	42
E3 (13)	30	26.5 ± 5.7	− 7	97 ± 12	23	41
	45	25.7 ± 7.4	− 10	103 ± 14	13	35
S3 (20)	30	2.6 ± 0.4	− 16	18 ± 16	122	7
	65	2.4 ± 0.3	51	17 ± 10	100	6
S1 (21)	30	7.2 ± 1.7	− 14	− 12 ± 12	− 164	69
	80	5.7 ± 1.4	19	− 13 ± 14	− 146	161
S2 (16)	25	30.8 ± 3.4	− 17	121 ± 05	2	59
	38	21.9 ± 2.7	13	120 ± 05	32	44
S4 (17)	25	6.0 ± 0.4	16	81 ± 05	80	9
	28	4.9 ± 0.8	18	− 108 ± 13	− 69	7

Table 3
As Table 2 but for the K_1 currents in the Santa Barbara Channel

Mooring (Station)	Instrument depth (m)	RMAJ (cm/s)	EPS (%)	Major axis orientation (degrees)	Phase (degrees)	Signal to noise ratio
W1 (02)	30	4.8 ± 0.0	− 34	− 37 ± 01	− 102	14
	100	5.6 ± 0.0	3	− 40 ± 00	− 131	15
W2 (03)	30	2.2 ± 0.1	− 35	− 38 ± 06	− 123	6
	100	3.6 ± 0.4	− 24	148 ± 04	3	8
	200	2.9 ± 0.7	− 11	0 ± 13	142	8
	350	1.9 ± 0.5	− 1	− 7 ± 11	155	10
W3 (04)	30	2.9 ± 0.1	− 42	− 37 ± 05	− 135	6
	100	3.0 ± 0.6	− 16	− 18 ± 08	− 160	14
	250	2.5 ± 0.2	− 17	13 ± 08	105	5
W4 (24)	8	4.9 ± 0.6	− 56	25 ± 08	− 118	9
(05)	30	4.3 ± 0.5	− 43	− 6 ± 05	− 128	22
	65	5.6 ± 0.4	− 41	− 18 ± 02	− 141	38
C1 (06)	30	3.2 ± 0.1	− 25	3 ± 02	96	10
	105	0.9 ± 0.0	− 41	− 17 ± 06	76	7
C2 (23)	8	3.0 ± 0.5	− 57	− 164 ± 11	6	8
(07)	30	1.0 ± 0.3	− 0	159 ± 12	− 8	4
	105	1.1 ± 0.3	− 17	− 170 ± 19	− 3	3
	538	1.4 ± 0.1	56	5 ± 06	− 114	5
E1 (10)	21	3.8 ± 0.1	− 7	− 37 ± 01	− 128	9
(11)	76	4.5 ± 0.2	− 28	− 49 ± 04	− 110	11
	126	3.5 ± 0.2	− 18	145 ± 01	26	10
	176	4.0 ± 0.2	− 30	132 ± 02	17	10
	246	2.3 ± 0.5	− 26	112 ± 13	45	3
E2 (12)	30	7.7 ± 1.1	− 17	114 ± 09	56	13
	80	10.6 ± 1.0	− 22	117 ± 05	54	21
E3 (13)	30	20.0 ± 1.4	− 28	86 ± 04	60	30
	45	19.1 ± 3.3	− 7	94 ± 10	53	25
S3 (20)	30	6.4 ± 0.2	− 60	80 ± 02	− 94	12
	65	1.6 ± 0.2	− 29	141 ± 07	− 38	5
S1 (21)	30	4.5 ± 0.0	− 9	− 12 ± 01	− 94	51
	80	5.3 ± 0.0	− 21	− 22 ± 01	− 88	24
S2 (16)	25	10.8 ± 1.1	7	121 ± 04	− 13	21
	38	8.5 ± 0.1	19	137 ± 01	5	21
S4 (17)	25	17.8 ± 0.3	− 6	76 ± 02	− 95	26
	28	11.5 ± 0.2	− 3	76 ± 02	− 93	15

a substantial fraction of the shelf width. Smaller but comparable tidal particle excursions occur all along the narrow southern shelf. The large tidal excursions, the large spatial gradients, and the shallowness of the waters on the southern shelf near the inter-island passages indicate that these regions are prime mixing zones. Furthermore, the rugged coastline of the channel islands with its many headlands, coves, and

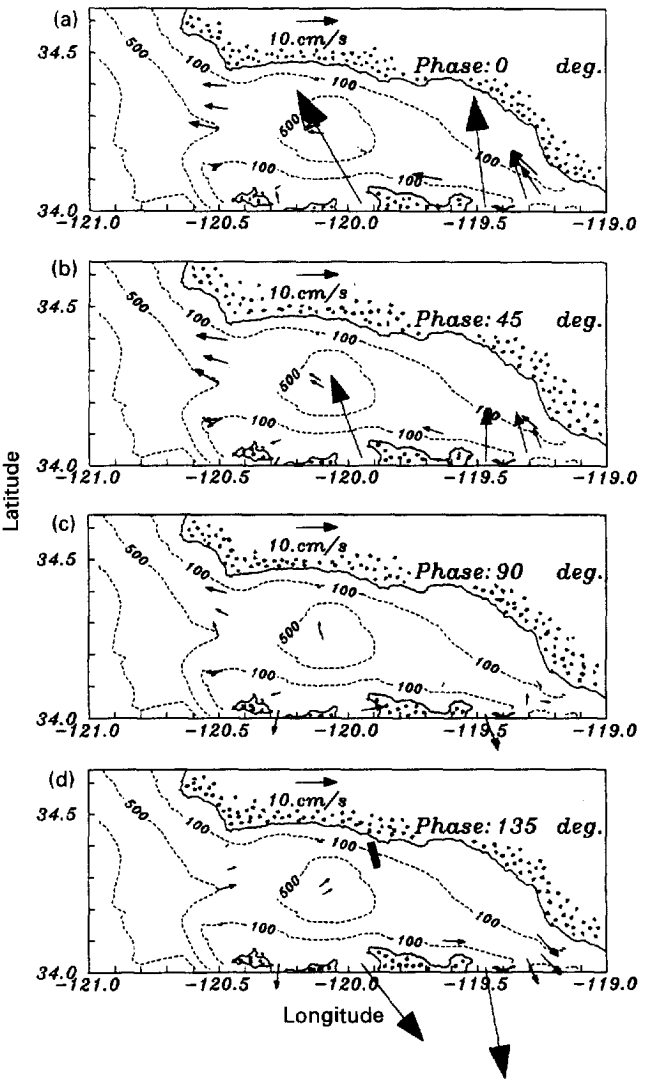

Fig. 7. Snapshot of near surface M_2 currents. Phase 0 refers to the time of predicted local M_2 high water (Santa Barbara, Greenwich phase 156.4°).

offshore rocky outcroppings facilitates tidal and residual eddies that can enhance particle dispersion (Zimmerman, 1986). Geyer and Signell (1990) and Wolanski et al. (1984) describe such small scale tidal features near a headland off Massachusetts and near narrow passages off Australia, respectively.

5.2. Vertical variability

The predictable tidal currents shown in Figs. 5–7 contain both barotropic and baroclinic contributions. They are in phase with the local sea level which distinguishes them from the intermittent tidal currents. In order to distinguish barotropic from baroclinic motions for both the predictable and the intermittent tidal currents, I here analyze data from a mooring that contained 7 current meters. The mooring was maintained for 62 days in 1983 at the center of the western entrance (near station 3 in Fig. 1). It contained instruments at 30, 65, 100, 135, 205, 275, and 350 m depth. Simplifying the discussion, I here and in the following discuss currents along the semi-major axis of the M_2 tide only. Fig. 8a shows a time series of the vertically averaged sea level coherent currents. I define this vertical average as the barotropic current. Baroclinic tidal currents result after the barotropic current (Fig. 8a) is removed from each individual current meter record. For clarity I show only 15 days

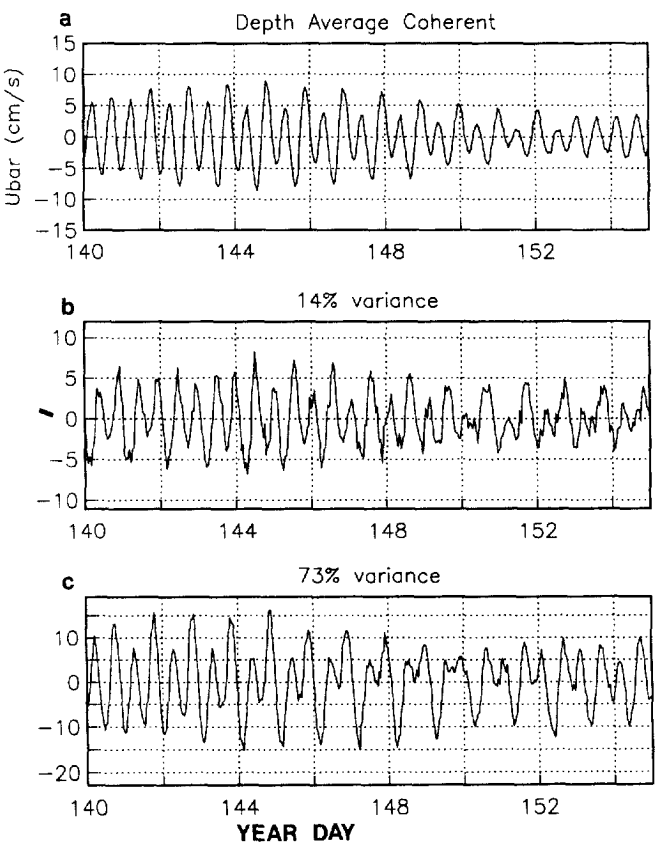

Fig. 8. Segment of the predictable 1983 currents that represent (a) barotropic, (b) mode 2 baroclinic, and (c) mode 1 baroclinic currents (station 3, see Fig. 1 for location).

of the 62 day long record. The barotropic currents are dominantly semi-diurnal ($\varepsilon = 1.67$) with a small diurnal inequality. The harmonic analysis of the barotropic current reveals a current amplitude of 4.8 cm/s (1.5 cm/s) for the dominant semi-diurnal M_2 (diurnal K_1) constituent. Maximum M_2 currents lag the M_2 high water in Santa Barbara 28° or by about an hour.

I next use variance estimates for currents in the tidal frequency band to estimate the respective contributions of baroclinic/barotropic and predictable/intermittent tidal currents to the overall variance. The total variance of the record is 297 $(cm/s)^2$ while the central limit theorem would indicate a total variance of about 322 $(cm/s)^2$, i.e., variance estimates using the central limit theorem are accurate to within 10%. Table 4 summarizes the results. The variance of the predictable and intermittent currents is 228 $(cm/s)^2$ and 94 $(cm/s)^2$, respectively. About 33% (95%) of the predictable (intermittent) tidal currents are baroclinic. Hence baroclinic motions contribute significantly to the predictable motions while barotropic motions contribute little to the intermittent motions. Put another way, about 49% (157 cm^2/s^2) of the total variance is barotropic of which 97% (152 cm^2/s^2) is predictable. Subsequently, 51% (165 cm^2/s^2) of the variance is baroclinic of which 46% is also predictable. In summary (Table 4), the variance is distributed about evenly between barotropic and baroclinic motions, however, almost half of the baroclinic variance is predictable in the sense that it has a phase that is fixed to the local sea level. To analyze the distribution of the baroclinic variance systematically, I next estimate vertical empirical orthogonal functions (EOFs).

An EOF analysis decomposes the baroclinic currents into ordered linear independent statistical modes that explain a fraction of the predictable baroclinic current variance. If the first few EOF modes explain a large fraction of this variance, then EOF analysis constitute a convenient tool to concisely discuss the data. Fig. 8c and b show the time series of the first and second EOF modes for the predictable currents, respectively. The first and second mode explain 73% and 14% of the variance in the tidal frequency band which is 76 cm^2/s^2 (Table 4). Instead of discussing all 7 current meter records, it thus suffices to discuss the first 2 modes that explain 87% of the variance. Note that the two EOF modes are baroclinic currents that are coherent with the sea level oscillations, i.e., they are deterministic, predictable, and have a phase that is locked to the barotropic tide.

Fig. 9 depicts the vertical structure of the eigen-vectors that correspond to the EOF amplitudes. They indicate that mode 1 represents a first mode baroclinic wave with

Table 4
Variance estimates (cm^2/s^2) in the tidal frequency band

	Barotropic	Baroclinic	Total
Predictable	152	76	228
Intermittent	5	89	94
Total	157	165	322

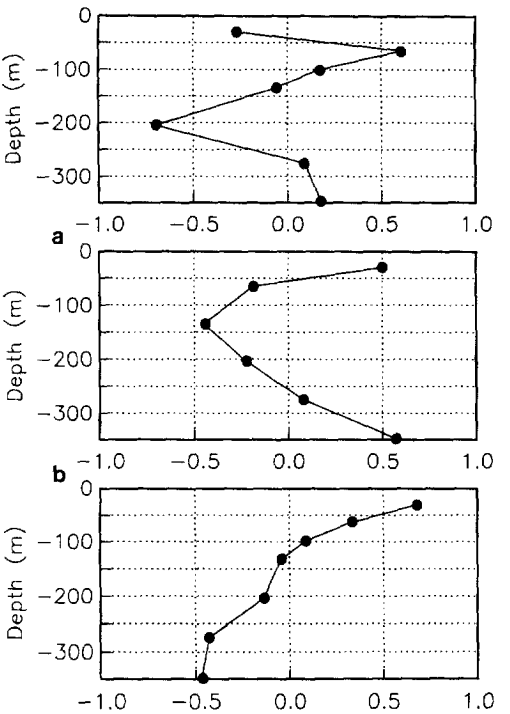

Fig. 9. Vertical structure of EOF mode 1 and 2 eigen vectors corresponding to the modal time series shown in Fig. 8b and c.

a zero crossing at about 125 m depth, i.e., surface and bottom currents are 180° out of phase. The mode 2 eigen-vector appears to represent a second mode baroclinic wave with almost identical surface and bottom currents that are in phase and a current of the same magnitude but 180° out of phase at 135 m depth. Harmonic analysis reveals that at the M_2 frequency the phase difference between the barotropic and the first mode baroclinic current is 14° or about $\delta t \sim 0.5$ h. A first estimate of the distance from the mooring to the internal wave generation region is $\delta x \sim c\ \delta t$. Here $c = (\Delta\rho g H/\rho)^{1/2}$ approximates the phase speed of a first mode internal gravity wave. For density $\rho = 1025\ \mathrm{kg/m^3}$, vertical density difference $\Delta\rho = 2\ \mathrm{kg/m^3}$, upper layer depth $H = 100$ m, and gravitational acceleration $g = 9.81\ \mathrm{m/s^2}$ this phase speed is about 1.4 m/s, i.e., $\delta x \sim 2.5$ km. It is this very short distance of the mooring from the generation region that probably ensures the detection of a phase-locked internal tide.

Figs. 10 and 11 show the temporal and vertical variability, respectively, of the currents that are not coherent with the sea level at Santa Barbara. Note that these intermittent currents have at times a sizable barotropic component that is about 4–5 cm/s strong (Fig. 10a). While some of this variance is certainly due to inertial oscillations, a major part of the variance is tidal. A harmonic analysis of this time series indicates, however, that no constituent has an amplitude above the noise level

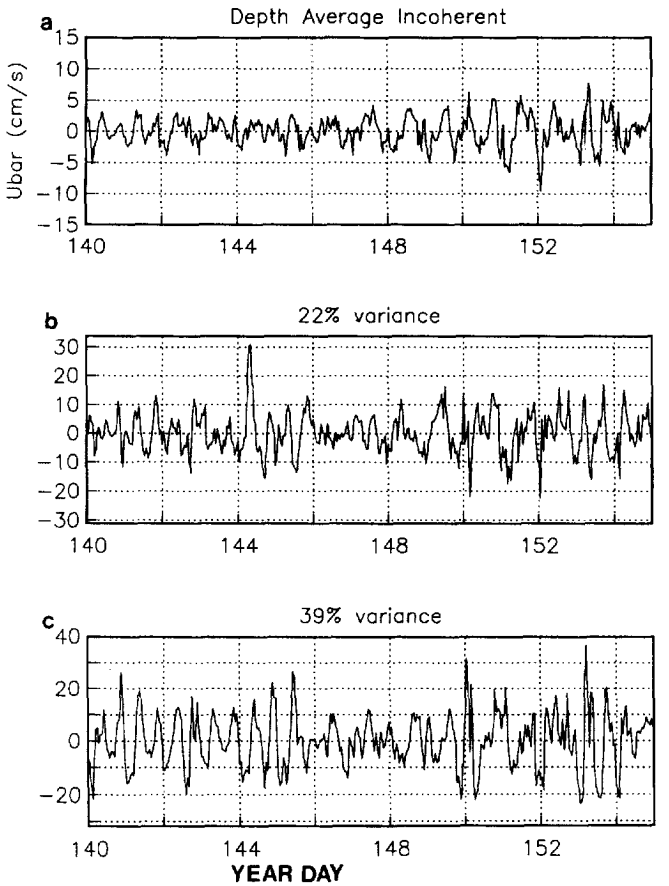

Fig. 10. As Fig. 8, but for the intermittent currents.

(not shown). We suspect that the small barotropic variance of the intermittent currents results from the definition that the vertical average of 7 current meters represents the barotropic flow. Nevertheless, the two largest EOF modes explain 39% and 22% of the total variance which is about 89 cm^2/s^2 (Table 4). While the spatial structure of the first EOF mode of the sea level incoherent currents (Fig. 11c) resembles that of the sea level coherent mode (Fig. 9c), the temporal variability is highly erratic (Fig. 10c) as one would expect from intermittent tidal currents.

The location of the zero-crossing in the first and second vertical EOF modal amplitudes reveals similarities and differences between deterministic and intermittent tidal currents. For mode 1 the flow changes direction at 100–150 m depth for both deterministic and intermittent tide. A CTD section across the western channel entrance shows that this depth is just below the pycnocline (Fig. 12). The "upper" layer is thus a layer that is strongly and continuously stratified while the "lower" layer is

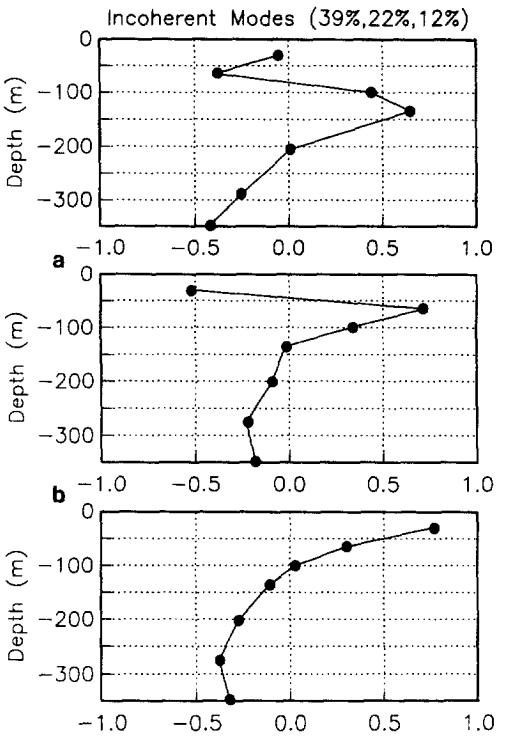

Fig. 11. As Fig. 9, but for the intermittent currents.

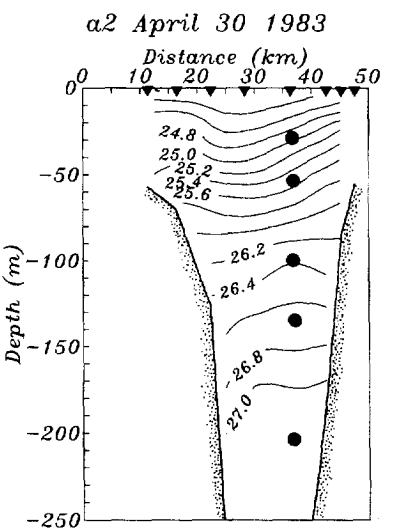

Fig. 12. Section of density across the western entrance of the Santa Barbara Channel. Also shown are the location of the current meter moorings used in the EOF analysis (Figs. 8–11).

also stratified but only weakly. Mode 2 is different as the intermittent tidal currents (Fig. 11) reflect a surface intensified mode that closely mirrors the temperature (not shown) instead of the density field.

5.4. Temporal variability

The presence of intermittent tidal currents causes the instantaneous tidal current amplitudes to vary in time. Spatial surveys of the subtidal circulation with towed or vessel-mounted ADCPs need to be detided using mooring and/or ADCP data along with an appropriate model of the spatial variability of the tidal currents (Candela et al., 1992; Münchow et al., 1992b). The choice of the model as well as the choice of the ship track depends strongly on the range and spatial variability of the instantaneous tidal currents. In order to obtain tidal amplitudes and phases as a function of time, I here apply a complex demodulation technique to the data (Rosenfeld, 1990). In practice the method is equivalent to a harmonic analysis with a single constituent applied successively over short periods of time of a longer record.

Fig. 13 shows the M_2 amplitudes of the semi-major axis as a function of time at a location in the central channel 30 m below the surface (station 7 in Fig. 1). Each estimate results from a harmonic analysis of a 2 day long subset of the year long record. Fig. 13a depicts the results for the original data while Fig. 13b and c depict the

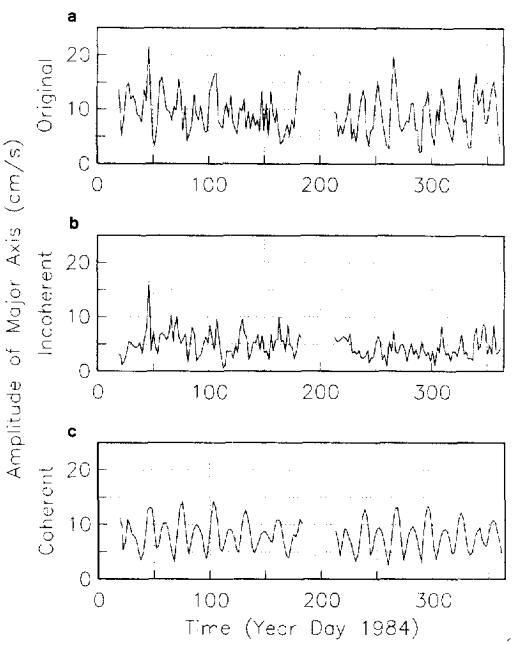

Fig. 13. Time series of M_2 current amplitudes determined from successive 2 day long records of the (a) original raw, (b) intermittent, and (c) predictable currents in the central deep channel (station 7 in Fig. 1).

results for the data that is incoherent and coherent with the sea level, respectively. The sea level coherent data reflects periodic variations of current amplitudes that vary between 2 and 8 cm/s. This beating effect results from the presence of the unresolved S_2 and N_2 constituents. In contrast both the original and the sea level incoherent data reveal M_2 tidal current amplitudes that vary without any apparent periodicity because the intermittent tidal currents are unpredictable. Note that the intermittent and the deterministic tide can add constructively at times such as near day 60. The current amplitude then reaches 12 cm/s even though the amplitude of the predictable M_2 tidal current at this location is only 3.8 cm/s (Table 2).

This analysis is repeated for all locations throughout the channel and Fig. 14 presents the maximum and the average current amplitudes. The amplitudes of the intermittent tidal currents are fairly uniform in space throughout the channel. In the temporal mean they are about 5 cm/s, however, their annual maximum in 1984 was about 15 cm/s (Fig. 14a). The spatial uniformity of the sea level incoherent velocity amplitude indicates that this part of the velocity record is indeed ambient noise that fills the entire channel. ADCP surveys need to resolve this tidal noise in order to archive accuracies of better than 15 cm/s in the estimation of subtidal currents. The amplitude of the sea level coherent as well as the raw data vary dominantly across the channel from 5 cm/s in the north to 25 cm/s in the south (Fig. 14b and c). Maximum tidal currents can reach amplitudes of about 50 cm/s. They occur at the eastern entrance as well as between the inter-island passages and reduce rapidly away from these locations. These currents, however, are deterministic. They can be predicted using either harmonic coefficients or the transfer functions between sea level and currents that I used to discuss the predictable currents.

6. Discussion

Our analysis of tidal currents in the Santa Barbara Channel revealed several regions with distinctly different tidal currents. In the central basin tidal currents were generally weak (<5 cm/s). Enhanced tidal currents occur where the Santa Barbara Channel is connected to the Santa Cruz and Santa Monica basins in the south. Near the eastern entrance tidal currents are about 15 cm/s which are forced by pressure gradients associated with the different dynamical response of the Santa Barbara Channel and the adjacent Santa Monica Basin. Larger tidal currents yet (25 cm/s) are observed in the shallow passages between the islands along the southern rim of the channel. These passages connect southern deep basins to the Santa Barbara Channel. It is not clear how far currents in excess of 25 cm/s extend into the channel. At one passage diurnal tidal currents exceed semi-diurnal ones by a factor of 5 while inside a passage 10 km to the east semi-diurnal currents exceed diurnal ones by a factor of 3. The particle excursions of such currents are comparable to the shelf width. Currents at these locations thus impact the horizontal mixing of particles. The enhanced tidal flow near the island passages interacts with strong subtidal flow (not shown) along the southern perimeter of the channel. The interaction of an oscillatory tidal flow with an ambient shear flow enhances particle dispersion (Zimmerman, 1986). I thus expect

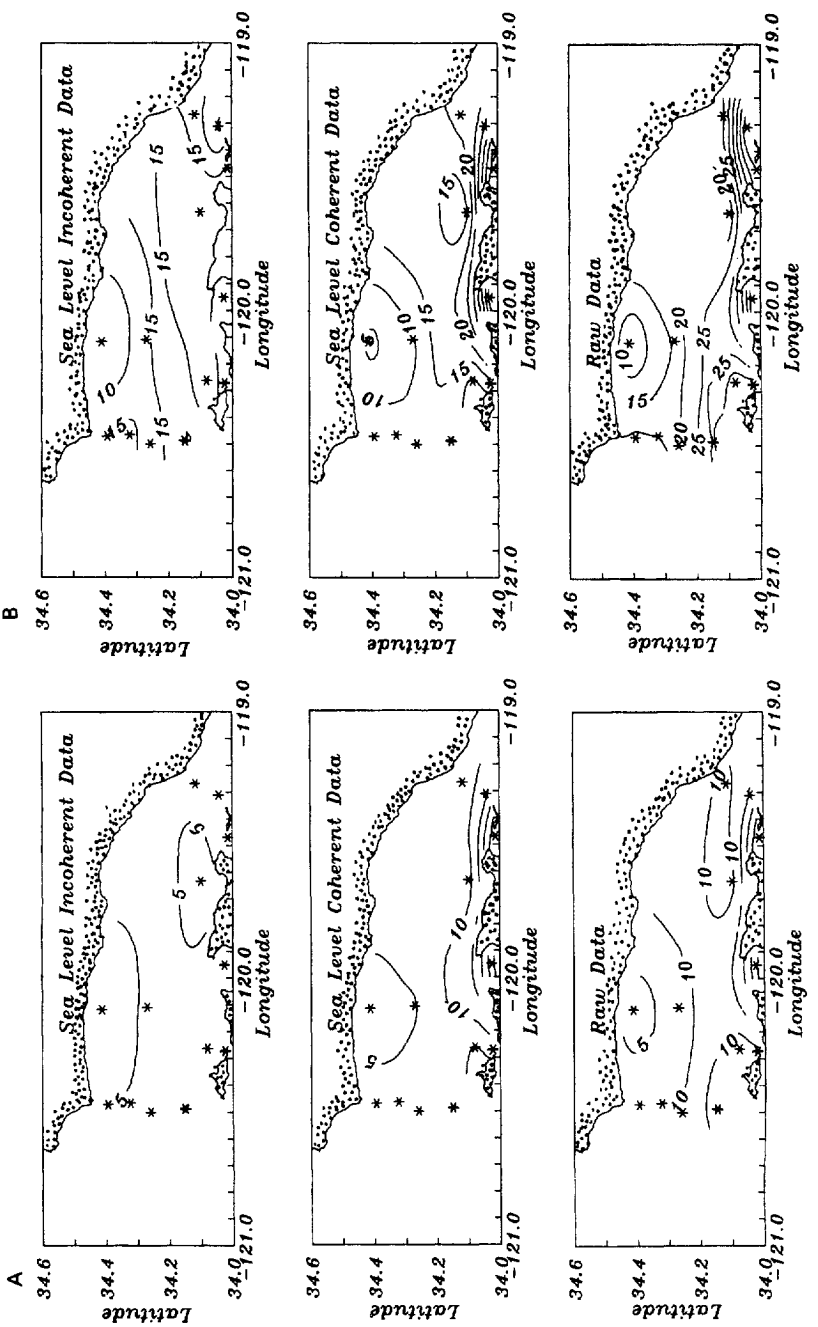

Fig. 14. Map of (a) average and (b) maximum M_2 current amplitude from successive harmonic analyses of 2 long current meter records. All data are from instruments within 60 m of the surface.

particles to separate faster on the southern shelf of the Santa Barbara Channel than in any other part of the channel.

A second finding of this study relates to the distribution of tidal variance between barotropic and baroclinic motions. It is often assumed that baroclinic tidal motions are intermittent and thus unpredictable. This, however, does not hold for the Santa Barbara Channel where a third of the total tidal variance is both baroclinic and predictable. At the western channel entrance baroclinic motions contribute substantially to the predictable tidal currents. The intermittent tidal motions are almost entirely baroclinic. An internal tide generation region is nearby and I hypothesize that the shelf break off Point Conception is such a region. The internal tide thus propagates into the channel where at times enhanced tidal currents can be found. The intermittent baroclinic tidal currents "fill" the Santa Barbara Channel with tidal "noise" that does not exceed 15 cm/s and in the temporal mean is about 5 cm/s. This observation has implications for the removal of tidal current from shipborne ADCP surveys.

Acknowledgements

This study was initially supported by a postgraduate fellowship of the Mineral Management Service (MMS). Nancy A. Bray supervised this work as part of Cooperative Agreement 14-35-0001-30571 between MMS and the Scripps Institution of Oceanography. She as well as Clinton Winant and Myrl Hendershott contributed to this study through continuing moral support. Sabine Harms generously provided Fig. 3. An anonymous reviewer improved the manuscript through detailed and thoroughly researched comments. The writing and final analysis was supported by institutional funds of the Institute of Marine and Coastal Sciences at Rutgers University.

References

Aubrey, D.G., Speer, P.E., 1985. A study of non-linear tidal propagation in shallow inlet/estuarine systems. Part 1: Observations. Estuar. Coast. Shelf Sci. 21, 185–205.

Battisti, D.S., Clarke, A.J., 1982. A simple method for estimating barotropic tidal currents on continental margins with specific application to the M_2 tide off the Atlantic and Pacific coasts of the United States. J. Phys. Oceanogr., 12, 8–16.

Bendat, J.S., Piersol, A.G., 1978. Engineering applications of correlation and spectral analysis. Wiley, New York.

Brink, K.H., Muench, R.D., 1986. Circulation in the Point Conception Santa Barbara Channel Region. J. Geophys. Res. 91, 877–895.

Candela, J., Beardsley, R.C., Limeburner, R., 1992. Separation of tidal and subtidal currents in ship-mounted acoustic Doppler current profilers. J. Geophys. Res. 97, 769–788.

Foreman, M.G.G., Freeland, H.J., 1991. A comparison of techniques for tide removal from ship-mounted acoustic Doppler measurements along the southwest coast of Vancouver Island. J. Geophys. Res. 96, 17007–17021.

Garrett, C., Petrie, B., 1981. Dynamical aspects of the flow through the Strait of Belle Isle. J. Phys. Oceanogr. 11, 376–393.

Geyer, R., Signell, R., 1990. Tidal flow measurements around a headland with a shipboard acoustic Doppler current profiler. J. Geophys. Res. 95, 3189–3197.

Giese, G.S., Hollander, R.B., 1987. The relationship between coastal seiches at Palawan Island and tide generated internal waves in the Sulu Sea. J. Geophys. Res. 92, 5151–5156.

Gill, A.E., 1982. Atmosphere-ocean dynamics. Academic Press, Orlando, FL.

Gunn, J.T., Hamilton, P., Hering, H.J., Kantha, L.H., Lagerloef, G.S.E., Mellor, G.L., Muench, R.D., Stegen, G.R., 1987. Santa Barbara Channel circulation model and field study – final report. Dynalysis of Princton, Report Number 92.1 and 92.2.

Helstrom, C.W., 1960. Statistical theory of signal detection. Pergamon Press, Oxford, UK.

Hendershott, M.C., Speranza, A., 1971. Co-oscillating tides in long, narrow bays: the Taylor problem revisited. Deep Sea Res. 18, 959–980.

Leaman, K.D., 1980. Some observations of baroclinic diurnal tides over a near-critical bottom slope. J. Phys. Oceanogr. 10, 1540–1551.

Münchow, A., Masse, A.K., Garvine, R.W., 1992a. Astronomical and nonlinear tidal currents in a coupled estuary shelf system. Cont. Shelf Res. 12, 471–498.

Münchow, A., Garvine, R.W., Pfeiffer, T.F., 1992b. Subtidal currents from a shipboard acoustic Doppler current profiler in tidally dominated waters. Cont. Shelf Res. 12, 499–515.

Munk, W., Snodgrass, F., Wimbush, M., 1970. Tides off-shore: Transition from California coastal to deep waters. Geophys. Fluid Dyn. 1, 161–235.

Noble, M., Rosenfeld, L.K., Smith, R.L., Gardner, J.V., Beardsley R.C., 1987. Tidal currents seaward of the Northern California continental shelf. J. Geophys. Res. 92, 1733–1744.

Ray, R.D., Mitchum, G.T., 1996. Surface manifestation of internal tides generated near Hawaii. Geophys. Res. Lett. 23, 2101–2104.

Rosenfeld, L.K., 1990. Baroclinic semi-diurnal tidal currents over the continental shelf off Northern California. J. Geophys. Res. 95, 22 153–22 172.

Sverdrup, H.U., 1926. The tides on the North Siberian shelf: Their bearing on the existence of land in the Arctic Sea, and their dynamics. J. Wash. Aca. Sci. 16, 529–540.

Taylor, G.I., 1921. Tidal oscillations in gulfs and rectangular basins. Proc. Lond. Roy. Soc. 20, 144–181.

Torgrimson, G.M., Hickey, B.M., 1979. Barotropic and baroclinic tides over the continental slope and shelf of Oregon. J. Phys. Oceanogr. 9, 945–961.

Wolanski, E., Imberger, J., Heron, M.L., 1984. Island wakes in shallow coastal waters. J. Geophys. Res. 89, 10 553–10 569.

Wunsch, C., 1975. Internal tides in the ocean. Rev. Geophys. Space Phys. 13, 167–182.

Zimmerman, J.T. F., 1981. Dynamics, diffusion, and geomorphological significance of tidal residual eddies. Nature 290, 549–555.

Zimmerman, J.T.F., 1986. A tidal whirlpool: A review of horizontal dispersion by tidal and residual currents. Neth. J. Sea Res. 20, 133–154.